International Journal of Microwave and Wireless Technologies

cambridge.org/mrf

Scattering parameters of a wet radome

Philipp J. Schmid[1,2], Maurizio Sartori[3], Marco Gabella[3], Matthias Renker[4], Daniel Wolfensberger[3], Mikko Kotiranta[1] and Axel Murk[1,2]

[1]Institute of Applied Physics, University of Bern, Bern, Switzerland; [2]Oeschger Centre for Climate Change Research, University of Bern, Bern, Switzerland; [3]Radar, Satellite and Nowcasting Division MDR, Federal Office of Meteorology and Climatology MeteoSwiss, Locarno, Switzerland and [4]Armasuisse Science and Technology, Bern, Switzerland

Research Paper

Cite this article: Schmid PhJ, Sartori M, Gabella M, Renker M, Wolfensberger D, Kotiranta M, Murk A (2025) Scattering parameters of a wet radome. *International Journal of Microwave and Wireless Technologies* **17**(5), 862–873. https://doi.org/10.1017/S1759078725000546

Keywords:
absorption; Fabry–Pérot interference; GRASP Physical Optics simulation; microwave measurement techniques and calibration; permittivity; radome; scattering; water; weather radar

Corresponding author: Philipp J. Schmid; Email: philipp.schmid@unibe.ch

Abstract

The radome of weather radars can be covered with a layer of water, degrading the quality of the radar products. Considering a simplified setup with a planar replica of the Swiss weather radars' radome, we measure and model analytically its scattering parameters, with and without water. The measured reflectance of the dry radome replica agrees well with the one modeled according to the manufacturer specifications. Water forms droplets on the hydrophobic surface, but water films thicker than 1 mm can be created. Meteorologically more realistic thinner water films are expected on old radomes that have become hydrophilic with aging. Using hygroscopic silk and cotton tissues, we empirically imitate water films as thin as less than 0.1 mm. The measurements align with the simple analytical model of uniform plane wave incidence on the radome and water film but could be further improved by taking refraction and bending of the radome replica into account. Simulations with the General Reflector Antenna Software Package (GRASP) from TICRA complement the study for a representative setup with a spherical radome.

Introduction

The Swiss weather radar network comprises five polarimetric C-band Doppler radars [1], operating at frequencies between 5430 and 5468 MHz. All five radars have a center-fed parabolic dish antenna surrounded by a spherical radar dome (radome) to protect against adverse environmental effects, see Fig. 1. The radome has a sandwich type design consisting of two fiberglass composites enclosing a low-density foam core. Thickness and dielectric properties of the three layers are chosen such that the radome is as transparent as possible at the working frequency of the radar. The outermost layer is covered with a hydrophobic gelcoat layer that protects the radome from erosion damage. The setup is typical for weather radars [2, 3].

When water deposits on the radome, the resulting multilayered structure *skin-core-skin-coating-water* has different electrical properties than the dry radome. The water attenuates the signal and modifies its phase, broadens the antenna pattern, adds an offset to the system noise floor level, can alter the pointing accuracy and causes depolarization, and consecutively degrades the quality of the radar products [4–8]. In practice, the accumulation of water on the radome is counteracted with (super-)hydrophobic properties of the coating. These coatings, with their low surface energy, enhance the runoff and the formation of droplets and rivulets, eventually reducing the transmission loss as compared to hydrophilic surfaces [5, 9–12]. However, the hydrophobic properties tend to fade with aging due to the adhesion of dirt from pollutants, erosion by ultraviolet radiation and other factors [5]. The degradation can become significant after time spans of the order of months [8, 13]. More durable coatings are being developed [14–16].

Given its operational relevance, the literature focuses on liquid water precipitation coverage. Ice and snow are less critical for the operational system, because their dielectric properties are closer to the one of air [17]. However, when a thick pack of ice and snow starts melting, a liquid water film of relevant thickness can form and high transmission losses are observed [8, 9, 18].

Selected references are the following. Analytical work is published for hydrophilic [19, 20] and hydrophobic surface properties [7, 11, 13]. Measurements under conditions of natural rain are documented in [4, 8, 9, 13, 21–26]. Experiments with artificial setups were conduced by [5, 6, 10, 12, 27–40]. Other authors focus on simulations [13, 36, 39, 41, 42] or make efforts to correct wet radome biases in real time [13, 19, 23, 26, 37, 42–50].

In this article, we investigate the scattering parameters of the radome of the Swiss weather radars at C-band, under dry and wet conditions. The findings shall help the operational monitoring of the weather radars, and contribute to developing methods for mitigating the adverse effects of the water in real time.

© The Author(s), 2025. Published by Cambridge University Press in association with The European Microwave Association. This is an Open Access article, distributed under the terms of the Creative Commons Attribution-NonCommercial-NoDerivatives licence (http://creativecommons.org/licenses/by-nc-nd/4.0), which permits non-commercial re-use, distribution, and reproduction in any medium, provided that no alterations are made and the original article is properly cited. The written permission of Cambridge University Press must be obtained prior to any commercial use and/or adaptation of the article.



Figure 1. The antenna system of the Swiss weather radars. The figure shows the 4.05 m parabolic dish antenna with 1.524 m focal distance inside of the spherical radome with 6.5 m outside diameter. The reflector surface has an 0.92 m offset from the center of the radome. The analogue and digital receivers are installed on the antenna counterweight (receiver-over-elevation box). The transmitter and the control cabinets are located in a separate room.

Using a simplified setup with a flat replica of the radome of the Swiss weather radars, we test the scattering parameters of the dry and wet radome empirically. The measurements, described in Section "Description of the measurements", are compared to the analytical model introduced in Section "Analytical model for flat radome". The results are presented in Sections "Dry material properties" and "Scattering parameters of the wet radome". To complete the study, Section "Physical Optics antenna simulations" concludes with simulations for a representative setup with spherical radome, using the *General Reflector Antenna Software Package (GRASP)* from TICRA.

An earlier version of this paper was presented at the *18th European Conference on Antennas and Propagation (EuCAP, Glasgow 2024)* and was published in its Proceedings [51]. This article completes the work with more and better calibrated measurements of all four scattering parameters, in particular, using fine silk and cotton tissues to empirically imitate thin water films. The experiments are performed with a refined measurement setup that is more stable, better aligned, and has additional absorbers to reduce ground reflections. Given the reflection and transmission measurements, we apply Poynting's theorem to compute the fraction of energy that is absorbed by the wet radome. Moreover, we analytically link the thicknesses of the measured water layers to certain rain rates (available in practice for the operational Swiss weather radars). We also updated the representative antenna simulations with respect to the conference paper. Finally, we aimed at clarifying the model assumptions and experiment conditions, also addressing effects due to refraction and bending of the radome replica in the experiment.

Analytical model for flat radome

The radome represents a stack of material layers, each with uniform thickness, enclosed by air. The materials are assumed to be linear, homogeneous, and isotropic. Solving the accordingly simplified Maxwell's equations for time-harmonic fields, in each layer, in Cartesian coordinates, each frequency component of the spectrum is given by a superposition of plane waves. Assuming the layers are infinitely extended, and ignoring multiple reflections outside the radome, a particular superposition consists of two linearly polarized uniform plane waves propagating along (+) and against (−) the z-axis indicated in Fig. 2a. Considering the electric field at the bottom interface of the radome (toward port 1 of the vector network analyzer), let us denote the complex amplitudes of the two contributions with $E_1^{\pm}(\nu)$. Similarly, we define $E_2^{\pm}(\nu)$ at the top interface of the (wet) radome. The outgoing fields (E_1^-, E_2^+) relate to the incoming fields (E_1^+, E_2^-) via the scattering matrix

$$\begin{pmatrix} E_1^- \\ E_2^+ \end{pmatrix} = \begin{pmatrix} \mathcal{R} & \mathcal{T}' \\ \mathcal{T} & \mathcal{R}' \end{pmatrix} \begin{pmatrix} E_1^+ \\ E_2^- \end{pmatrix} . \tag{1}$$

The frequency-dependent scattering parameters combine the absorptive properties of the layers and the Fabry–Pérot interference effects. For our purposes, the characteristic impedance on both sides of the multilayered radome is the same (dry air). In this case, the *transmission responses* $\mathcal{T}$ and $\mathcal{T}'$ are equal. The *reflection responses* $\mathcal{R}$ and $\mathcal{R}'$ are in general similar only for symmetric (such as our dry radome replica) and for lossless multilayers. We now focus on monochromatic waves, set $E_2^- \equiv 0$ and assume the surrounding air is lossless. Evaluating Poynting's theorem for the domain $\mathcal{V}$ indicated in Fig. 2a, and averaging over one period of oscillation, yields

$$1 = |\mathcal{A}|^2 + |\mathcal{R}|^2 + |\mathcal{T}|^2 , \tag{2}$$

where the *absorptance* $|\mathcal{A}|^2$ represents losses due to Ohmic heating and polarization damping forces [52, p. 38]. Similarly we can set $E_1^+ \equiv 0$ instead and define the absorptance $|\mathcal{A}'|^2$. The absolute squares of reflection and transmission responses are called *reflectance* and *transmittance*. Here $|\mathcal{T}|^2$, $|\mathcal{R}|^2$, and $|\mathcal{A}|^2$ are referred to as *outgoing* transmittance, reflectance, and absorptance and represent weather radar transmission. The *incoming* counterparts $|\mathcal{T}'|^2$, $|\mathcal{R}'|^2$, and $|\mathcal{A}'|^2$ stand for weather radar reception. Note that Eq. (2) is independent of the extension of $\mathcal{V}$ in the plane orthogonal to the direction of propagation and only follows from the above-made assumptions about the material layers and because monochromatic uniform plane waves are transverse. For a more extended treatise of the model, see [53, pp. 173–191]. As to wet radomes, the model holds for water films of uniform thickness and is often used in similar work such as [9, 34].

Description of the measurements

Measurement setup

The manufactured radome replica is square-shaped with a side length of 1 m and features a 2-mm-thick epoxy border to contain the water. In the experiment, the replica is positioned horizontally, allowing the water to spread over its entire surface. The setup is shown in Fig. 2. On the one hand, the configuration facilitates the control over the water, as well as the monitoring of its amount and distribution on the radome surface. On the other hand, the geometry replicates the wet radome model proposed in [19], which describes the water distribution on hydrophobic spherical radomes exposed to steady and uniform rain. Assuming laminar flow, on the upper hemisphere of the radome, the model suggests a water film with uniform thickness

$$\ell_w(R, T) = \left(\frac{3aR\nu_w(T)}{2g} \right)^{1/3} , \tag{3}$$

where $g \approx 9.81\,\mathrm{m/s^2}$ is the gravitational acceleration, a is the radome radius, R is the rain rate, T is the water temperature, and $\nu_w(T)$ its kinematic viscosity [20]. The water's kinematic viscosity is linearly interpolated from the values given in [54, p. 758]. As it does for the real weather radar, in our experimental setup, the center of the beam intersects perpendicularly with the radome. The influence of the radome curvature is further addressed in the Physical Optics simulations presented in Section "Physical Optics antenna simulations".

In reality, hydrophobicity, surface roughness [20], wind, the presence of joints, and lightning rods, etc. will preclude the

https://doi.org/10.1017/S1759078725000546 Published online by Cambridge University Press

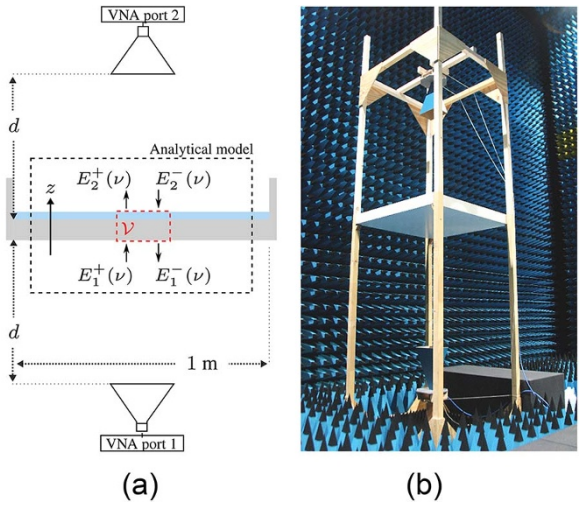


Figure 2. Analytical model and empirical realization of wet radome scattering at C-band. The analytical model is illustrated within the black-dashed contour line in Figure 2a. It comprises complex field amplitudes at the radome inside (bottom) and outside (top) interfaces, $E_1^{\pm}(\nu)$ and $E_2^{\pm}(\nu)$, with adjacent arrows that indicate the directions of propagation of the corresponding waves along the z-axis. In the experiment, a $1\,\mathrm{m} \times 1\,\mathrm{m}$ radome replica is centered between two rectangular horn antennas, the distance d from the surfaces of the radome replica, and connected to a two-port vector network analyzer (VNA). The red-dashed contour outlines the spatial domain $\mathcal{V}$ used for evaluating Poynting's theorem. Figure 2b shows a photo of the measurement setup used for the "film," "cotton," and "silk" experiments (see Section "Description of the measurements — Simulating a rain coverage in the laboratory") with $d = 104 \pm 0.5\,\mathrm{cm}$. A similar, but more provisional, wooden scaffold with $d = 126.5 \pm 1\,\mathrm{cm}$ was used in previous experiments, referred to as "droplets/film" (see Section "Description of the measurements — Simulating a rain coverage in the laboratory" and [51]). (a) Analytical model versus empirical realization of wet radome scattering. (b) Measurement setup with horn antennas, flat radome replica, and wooden scaffold.

formation of uniform water films, inducing waves [55], streaks, and directional differences in the amount of water on the radome [24, 45–47].

The radome replica is vertically centered between two rectangular horn antennas (*Pasternack 3.95–5.85 GHz WR187 standard gain horn antenna PE9861/NF-20*) with linear polarization and directive radiation pattern. In the experiment, the horns are used for frequencies from 3.5 GHz through 7 GHz. Simulations with GRASP at 3.5 GHz, 5.45 GHz, and 7 GHz indicate peak directivities of approximately 17 dB, 20 dB, and 22 dB and half-power beam widths around 26°, 17°, and 14°. The far-field distances are roughly 1.2 m, 1.9 m, and 2.4 m (controlled by the Rayleigh condition here). The horns are connected to a two-port vector network analyzer (*Keysight FieldFox N9951A*). The separation d between antenna and radome replica is motivated by several factors: simulated antenna pattern, estimated far-field distance of the antennas, size of the radome replica, and feasibility of the experiment scaffold. The latter is made of dry spruce wood [56, 57] and held together with metallic screws. Its influence on the measurements is not considered in full detail but will be removed to large extents by the soothing procedure described in Section "Scattering parameters of the wet radome — Spectrum for thin water films". The measurements are performed in an anechoic chamber to ensure frequency protection and to minimize multipath artifacts.

Calibration

Calibration is done in the absence of the radome replica but with both antennas attached, by means of "through" measurements for calibrating the transmission responses $\mathcal{T}$ and $\mathcal{T}'$, and "matched" and "short" measurements for calibrating the reflection responses $\mathcal{R}$ and $\mathcal{R}'$ in Eq. (1), see, e.g., [58, 59]. The "short" measurements are made with a $1\,\mathrm{m} \times 1\,\mathrm{m}$ wooden board with a thin aluminum sheet glued to one side. In the first step, this calibration plate is positioned such that the aluminum surface coincides with the bottom interface of the radome replica in the experiment. In the second step, the plate is flipped, such that the aluminum surface aligns with the top interface of the radome replica in the experiment with about 0.5 mm accuracy. However, notice that the wet radome reflection response $\mathcal{R}'$ pertains to the upper surface of the water, which is closer to the antenna than the upper interface of the radome replica. Because the antenna pattern is not a uniform plane wave but a divergent beam, we expect that the resulting reflectance measurements are slightly too high. Coupling simulations with GRASP suggest discrepancies lower than 0.04 dB for the considered frequencies from 3.5 GHz to 7 GHz and water layer thicknesses $\ell_w < 4\,\mathrm{mm}$.

In the experiment referred to as "droplets/film" (see Section "Description of the measurements — Simulating a rain coverage in the laboratory"), performed with a similar setup during a previous measurement campaign, only a small aluminum plate was at hand for the calibration of the reflection responses and S22 was not calibrated. The plate is placed in direct contact with the antenna to cover its aperture, and the measurements are corrected via coupling simulations in GRASP. The corrected reflectances are between 30 and 60 times higher than the uncorrected ones. Because the beam is more divergent at the low frequencies, the highest corrections apply here. Note that data from the "droplets/film" experiment are also presented in the conference paper [51], but the simulations and data processing have been revised for the current article.

Accuracy of the calibration method

The specified calibration technique is designed for uniform plane waves like the ones in the analytical model introduced in Section "Analytical model for flat radome". While uniform plane waves allow for a trackable formulation of the scattering problem with decent similarity with the measurements (as we shall see in Sections "Dry material properties" and "Scattering parameters of the wet radome"), a more comprehensive analytical description would approximate the antenna radiation pattern as a Gaussian. In particular, notice that the radome acts as a system element that refractively focuses the field (beam waist and radius of curvature), and quasi-optical beam transformation indicates that the *transmitted (reflected) beam is more (less) focused* [60, pp. 39–57]. That introduces a calibration bias, which refers to unperturbed beam growth and reflection at the aluminum calibration plate. Moreover, considering multiple reflections at the interfaces of the wet radome is fairly more involved than in the more simplistic model of uniform plane wave incidence. An analytical model that describes the interaction of a Gaussian beam with one flat material slab is given in [58].

Considering that the radome gets bent under the effect of gravity, by virtue of its own weight and due to the weight of the water, a curved interface forms and the effects of lensing (transmission) and mirroring (reflection) tend to become more relevant. Furthermore, the bending leads to an excess of water in the center of the radome, and because on-axis signal propagation is most relevant in our setup we expect a *shift of the Fabry–Pérot interference pattern* with respect to the same amount of water distributed

https://doi.org/10.1017/S1759078725000546 Published online by Cambridge University Press

in the form of a film with uniform thickness. Ignoring any curvature of the upper water surface, the effect of bending is evaluated by fitting to the power spectra of the measured scattering parameters with the analytical model presented in Section "Analytical model for flat radome", using the water layer thickness as the parameter of interest. Knowing the weight of the water, we compute the corresponding thickness ℓ_w of a water film with uniform thickness (see Section "Description of the measurements — Simulating a rain coverage in the laboratory") and use this value as initial condition for the optimization problem. The difference between the fitted and the computed water layer thickness, $\ell_w^{\text{fit}} - \ell_w$, suggests that bending is negligible for the dry radome replica and the meteorologically relevant thin water films, corresponding to the rigidity of the radome replica. With raising water volume on the radome, the difference tends to increase, but with considerable uncertainty. For $\ell_w \sim 3$ mm, the difference is between about one and two tenths of a millimeter. Establishing a geometrical model to describe the gravity-induced deformation, we can estimate the corresponding radius of curvature R of the wet radome replica. Taking $\ell_w \approx 3.6$ mm and $\ell_w^{\text{fit}} \approx 3.8$ mm, say, we get $R \approx 417$ m. It would be conclusive to model the refractive bias for both the flat and the bent radome replica.

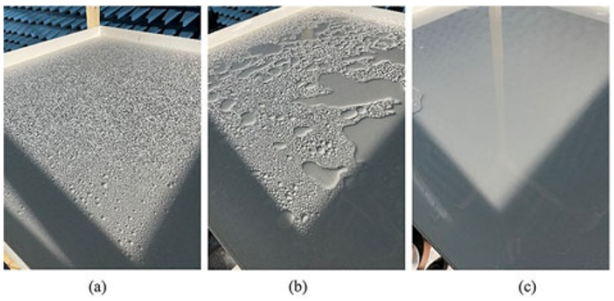


Figure 3. Photos of the experiment referred to as "droplets/film." The numbers represent the amount of water on the radome. Water accumulates on the hydrophobic surface as droplets (Figure 3a). As more water is sprayed, droplets coalesce into patches (Figure 3b). At this point, the water could be manually spread into a film (Figure 3c). We estimate a loss of 5 ± 4 g water during that process. The water film covers approximately $90 \pm 5\%$ of the radome, with only a few dry spots near its borders. The thickness of the water film over the central part of the radome is given by $\ell_w = m_w/(\rho_w A f) = 1.35 \pm 0.07$ mm, with $m_w = 1212 \pm 4$ g the mass of the water on the radome, $\rho_w \approx 1\,\text{kg/m}^3$ the water density, $A = 1\,\text{m}^2$ the radome surface area and $f = 0.90 \pm 0.05$ the fraction of the surface covered with the water film. Water deployed areas are visible on the bottom and in the left parts of the photograph. (a) 147.0 ± 0.4 g, (b) 1217.0 ± 1.2 g, and (c) 1212 ± 4 g.

Poynting's theorem in the experiments

In the experiment, the electromagnetic fields do not exclusively propagate along one axis and exhibit dependence also on the transverse coordinates. As a result, evaluating Poynting's theorem is more complex than for the monochromatic uniform plane waves in Eq. (2), and the spatial extent of the domain $\mathcal{V}$ becomes important. Vertically centering the radome replica between the two antennas, we aim to achieve that the portions of the wet radome that contribute to the scattering of signal into the receiving antenna are similar on reflection and transmission. However, a mismatch between the sensed domains is likely inevitable due to experimental limitations. Considering that the relevant domain is close to the antenna boresight axis (provided that the radome replica is sufficiently large to ensure that edge diffraction effects are negligible), and that the radome is relatively thin, the domain might be reasonably described with a cylinder and the flow of energy across its lateral faces be negligible. The domain is outlined in Fig. 2a (red-dashed).

In order to test the effect of edge diffraction, dedicated transmission measurements are made in the presence of the aluminum calibration plate. The data are more than 30 dB lower than the observed free-space transmission between the antennas (not shown here) and at least 10 dB less than in the performed wet radome tests.

Supposing that the Poynting vectors in the wet radome and calibration measurements were parallel, calibration would allow to approximately compute the absorptance like in Eq. (2). However, the radome replica refocuses the radiation and thereby causes a bias with respect to calibration (Section "Description of the measurements — Accuracy of the calibration method"), and which should be estimated.

Simulating a rain coverage in the laboratory

In the empirical tests presented here, we use demineralized water as a reproducible substitute for clean rain. Pure water is a nonmagnetic, nonconductive dielectric, governed by *orientation polarization* at the microwave frequencies used in this study [61]. In nature, water is typically an electrolytic solution with ionic impurities, giving rise to a nontrivial conductivity [17, 62].

For wetting the radome, we use a handheld water spray bottle with relatively homogeneous beam. The amount of water on the radome is determined by weighing the spray bottle before and after spraying, using a laboratory scales with measurement accuracy of 0.1 g (*Mettler PE 6000 precision balance*). Assuming the water deposits on the radome as a uniform film, its thickness is computed like $\ell_w = m_w/(\rho_w A)$, from the water mass m_w with water density $\rho_w \approx 1\,\text{kg/m}^3$ and surface area $A = 1\,\text{m}^2$ of the radome replica. To compare the measurements with the analytical model introduced in Section "Analytical model for flat radome", we use the dielectric properties of the water given in [63]. Effects of evaporation are not considered and deemed to be negligible with respect to the sum of other measurement uncertainties.

The first experiment (denoted "droplets/film") is done at temperature $T = 25 \pm 1$°C, see Fig. 3 and [51]. Because the water deposits in the form of droplets on the hydrophobic radome surface (Fig. 3a), the computed thickness has no strictly quantitative meaning in that case but simply represents the amount of water present. We spray water until parts of the droplets reconnect to patches with diameters of several centimeters (Fig. 3b). At that point, we smear out the water to a continuous film with thickness $\ell_w \approx 1.35$ mm (Fig. 3c).

In the second experiment (referred to as "film"), even thicker water films are generated at $T = 22 \pm 1$°C.

With reference to Eq. (3), however, we conclude that for typical rain rates only very thin water films are of practical meteorological interest. In order to empirically simulate sufficiently thin water sheets, we use a supplementary material layer of fine hygroscopic silk or cotton tissue on the radome. For both experiments, the water temperature is $T = 23 \pm 0.5$°C. More measurements are made with thin paper tissue [51].

In the experiment "droplets/film," the horns are the distance $d = 126.5 \pm 1$ cm away from the radome. In the other experiments ("film," "cotton," and "silk"), the separation is $d = 104 \pm 0.5$ cm (Fig. 2a). The difference should hardly affect the calibrated measurements.

https://doi.org/10.1017/S1759078725000546 Published online by Cambridge University Press

Table 1. Material parameters of core, skin, and coating of the planar radome replica. Taking the relative permittivity $\epsilon_d = \epsilon_d' - i\epsilon_d''$ to be independent of frequency, the table shows the supposed values of ϵ_d' and of the loss tangent $\tan(\epsilon_d''/\epsilon_d')$. The thickness of each layer is also given. The materials are considered nonconductive and nonmagnetic

Layer	ϵ_d'	$\tan(\epsilon_d''/\epsilon_d')$	Thickness (mm)
Core	1.065 ± 0.005	0.004 ± 0.001	38.0 ± 0.2
Skin	4.1 ± 0.1	0.025 ± 0.005	0.4 ± 0.1
Coating	Similar to skin	Similar to skin	~ 0.1

Dry material properties

By reason of Fabry–Pérot interference effects between the interfaces of the radome and the water, knowledge about the electromagnetic properties of the dry radome is prerequisite for modeling and interpreting the scattering parameters of the wet radome. In Section "The flat radome replica", therefore, we introduce and test the properties of the flat radome replica. In Section "Tissues for the simulation of a water film", we describe the properties of the cotton and silk tissues that are used in the experiment.

The flat radome replica

Composition according to manufacturer

The radome replica has a symmetric sandwich structure made up of the layers *coating-skin-core-skin-coating*, whereas the real radome of the Swiss weather radars lacks an inner coating (see Section "Introduction"). The core of the radome replica is made of *AIREX® R82*. The skin comprises two E-glass fiber layers, parallel stacked and clotted with *Gremopal 136.15/UB polyester resin*. The coating is *white (RAL900) NUVOPOL® Gelcoat 21-50 TSP*. Table 1 summarizes the material parameters of the layers. As the dielectric properties of skin and coating are similar, we combine them in the model, considering the three-layered geometry *skin-core-skin* with skin of thickness 0.5 ± 0.1 mm.

Measurements under dry conditions

To assess the electromagnetic characteristics of the flat radome replica, we measure its reflectance under dry conditions. Measurements over a broad frequency range facilitate the comparison with theoretical predictions. Our equipment allows measurements at C-, K-, and Ka-band. Figure 4 shows $|\mathcal{R}|^2$ (yellow). The reverse quantity $|\mathcal{R}'|^2$ is practically identical (not shown), confirming, as stated in Section "Analytical model for flat radome", that the multilayered radome is very symmetric. The dashed yellow line is the modeled reflectance with the manufacturer specifications in Table 1. Measurement and model are in a satisfactory agreement, and as expected the radome has a low reflectance at the working frequencies of the Swiss weather radars. However, the reflection notch is at frequency $\nu \approx 5800$ MHz rather than at $\nu \approx 5450$ MHz.

For C-band, we utilize the setup in Fig. 2b, but in order to minimize reflections from the background, the reflectance measurements shown here are obtained before mounting the antenna for VNA port 2 and the supporting upper parts of the scaffold. Reflectance measurements with the full setup are shown in Fig. 5 (yellow). At K- and Ku-bands, we use similar laboratory setups with a K-band corrugated conical horn antenna specified for the frequency range from 18 to 26.5 GHz, and a similar Ka-band horn between 26.5 and 40 GHz. The K-band antenna even allowed for decent measurements down to 16 GHz. Similar but more preliminary tests are shown in [51].

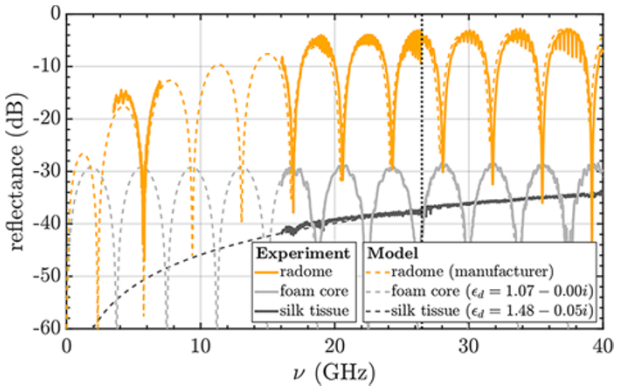


Figure 4. Measurements of the radome reflectance $|\mathcal{R}|^2$, shown on a logarithmic scale versus frequency ν (yellow), and modeled reflectance according to the manufacturer specifications provided in Table 1 (dashed yellow). The measurements are conduced using three different setups. For the 3.5–7 GHz range, the setup from Figure 2 is used without the upper half of the scaffold. At the higher frequencies, two corrugated conical horns are used: one for 16–26.5 GHz and the other for 26.5–40 GHz (marked by the vertical black-dotted line at 26.5 GHz). For the latter two frequency ranges, the figure also shows the measured reflectance of a material sample of the radome foam core (light gray) and the silk tissue used to create thin water films (black). The dashed curves are the fitted one-slab-models, optimizing the relative permittivity ϵ_d given the thickness of the foam core sample (38.74 ± 0.06 mm) and of the silk tissue (0.100 ± 0.002 mm). The resulting estimates of ϵ_d are shown in the legend.

Figure 4 also shows calibrated reflectance measurements of a material sample of thickness 38.74 ± 0.06 mm of the radome foam core (light gray). Fitting the measurements with a one-slab-model analogous to the multilayer model of Section "Analytical model for flat radome" (dashed light gray), we can estimate the material's relative permittivity $\epsilon_d = \epsilon_d' - i\epsilon_d''$ (assumed frequency independent). The nonlinear least squares problem is solved with a trust-region method algorithm, using as initial condition the value of ϵ_d given in Table 1, and bounding the optimization to values $\epsilon_d' \geq 1$ and $\epsilon_d'' \geq 0$. That yields $\epsilon_d' \approx 1.07$ and $\tan(\epsilon_d''/\epsilon_d') \sim 10^{-7}$. The measured value of ϵ_d' is similar to and the losses are even lower than the manufacturer specifications in Table 1.

Tissues for the simulation of a water film

Table 2 summarizes the measured material properties of the cotton and of the silk tissues. The thickness of each tissue is measured with a digital height gauge (*TESA MICRO-HITE + M/M600*) and a thin gauge block to minimize the deformation of the tissue during the measurement. The densities are deduced from thickness, weight, and surface area. The *solid volume fraction* [64] of the tissues is estimated from the change in volume upon immersing a piece of tissue into a measuring cylinder filled with water. Table 2 also indicates the relative permittivities of the cotton and of the silk tissues, empirically estimated by fitting the measured reflectance of the tissues. This method is similar to that used for the material sample of the radome foam core in the previous section. Figure 4 shows the measured and fitted reflectance of the silk tissue (solid and dashed black). The measurements are performed at room temperature and relative humidity of about 50%. The results are consistent with previous studies [64–66].

https://doi.org/10.1017/S1759078725000546 Published online by Cambridge University Press

Table 2. Material properties of the cotton and of the silk tissues. Assuming the relative permittivity $\epsilon_d = \epsilon_d' - i\epsilon_d''$ to be frequency independent, the table shows the values of ϵ_d' and of the loss tangent $\tan(\epsilon_d''/\epsilon_d')$ as estimated from the measurements. The tissues are considered as nonconductive and nonmagnetic dielectrics

Specification	Cotton	Silk
Construction	Plain weave	Plain weave
Thickness (mm)	0.207 ± 0.002	0.100 ± 0.002
Density (g/cm^3)	0.33 ± 0.01	0.24 ± 0.01
Solid volume fraction	0.25 ± 0.03	0.27 ± 0.06
ϵ_d'	1.53	1.48
$\tan(\epsilon_d''/\epsilon_d')$	0.08	0.03

Scattering parameters of the wet radome

We present results of the wet radome experiments described in Section "Description of the measurements — Simulating a rain coverage in the laboratory". Focusing on thin water films, Section "Spectrum for thin water films" provides an overview of the measurements at frequencies from 3.5 GHz through 7 GHz. The Section "Scattering parameters at the working frequencies of the Swiss weather radars" focuses on the frequencies 5.4–5.5 GHz which are of particular interest for the Swiss weather radars, summarizing the scattering parameters statistically in the outgoing and incoming directions within that frequency interval.

Spectrum for thin water films

Figure 5 shows the measured (continuous) and the modeled (dashed) transmittance and reflectance, and the computed absorptance according to Eq. (2) for both dry and wet radome up to 7 GHz. The measurements are conduced at the water temperature $T = 23 \pm 0.5$°C, using the full setup described in Section "Description of the measurements — Measurement setup" with both antennas mounted. After the calibration (see Section "Description of the measurements — Calibration"), the values are smoothed with a low-pass filter to eliminate standing wave effects due to multiple reflections between the two antennas and the radome, which are not removed with the calibration measurements because the wet radome causes a change in phase. The artifacts at the band edges of the smooth data result from the low-pass filtering. An example of calibrated data before the smoothing procedure is shown in Fig. 5, for the measurements with water film thickness $\ell_w \approx 0.2267$ mm computed according to Section "Description of the measurements — Simulating a rain coverage in the laboratory" (dotted magenta): the local maxima of the spectra are separated by $\Delta\nu \approx 0.1$ GHz. This corresponds to the spacing between the resonant frequencies in a resonator of length $L = c/(2\Delta\nu) \approx 1.5$ m, which matches the distance between the wet radome and the waveguide section of the horn antennas. The cutoff for the low-pass filtering is set to $1/(2\Delta\nu) = 0.5\,\text{GHz}^{-1}$. The resonance effects could be eliminated with a time gating.

Likely due to additional background reflections, the measured reflectance of the dry radome (orange) differs slightly more from the model than similar measurements taken before installing the upper half of the scaffold (yellow line in Fig. 4), near the reflection notch at frequency $\nu \approx 5800$ MHz. It is important to ensure meticulous positioning and alignment of antenna, radome, and aluminum calibration plate.

The thinnest water film is measured using the silk tissue ($\ell_w \approx 0.0171$ mm computed water film height). The other measurements

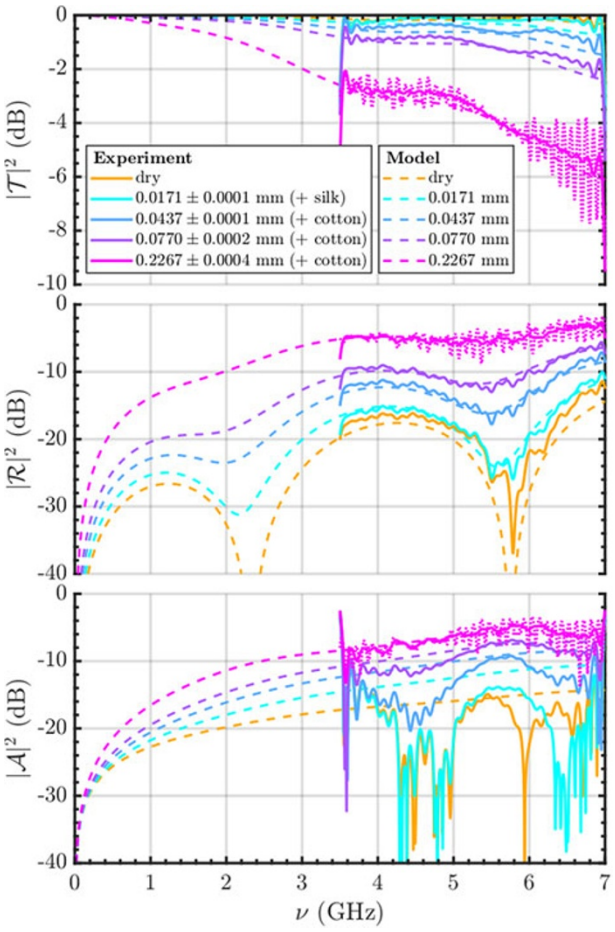


Figure 5. Measured (continuous) and modeled (dashed) transmittance $|\mathcal{T}|^2$, reflectance $|\mathcal{R}|^2$, and absorptance $|\mathcal{A}|^2$ in the outgoing direction (corresponding to radar transmission) for dry and wet radome versus frequency ν, at $T = 23 \pm 0.5$°C. Measurements are taken using the full setup from Section "Description of the measurements — Measurement setup" (Figure 2) with both antennas attached. The thinnest water film is measured with the silk tissue on the radome (cyan), the other ones with the cotton tissue (blue, purple, and magenta). The model refers to the computed water heights, ignoring the presence of the tissue.

are done with the cotton tissue ($\ell_w \approx 0.0437$ mm, $\ell_w \approx 0.0770$ mm, and $\ell_w \approx 0.2267$ mm). We ignore the presence of the tissue when computing the water height, accepting the following systematic errors.

Regarding the measurement with computed water film thickness $\ell_w = 0.2267 \pm 0.0004$ mm (see Fig. 5), the water surface is estimated to be 0.052 ± 0.006 mm higher (product of the thickness and of the solid volume fraction of the cotton tissue given in Table 2), i.e. about 0.279 ± 0.006 mm. More precisely, two layers should be considered separately: a layer of thickness 0.207 ± 0.002 mm with *effective* dielectric properties [57, 67] (assuming that the thicknesses of dry and wet cotton tissue are the same) and a water layer of thickness 0.072 ± 0.007 mm above the wet tissue (provided that the tissue does not float in the water). Concerning the measurements with computed water film thicknesses $\ell_w \approx 0.0171, 0.0437, 0.0770$ mm, the water heights are less than the thickness of the tissue, even after accounting for the water level increase due to the tissue solid volume fraction. However, since the tissues are hygroscopic, water is absorbed throughout the tissue, and so the water surface cannot be precisely defined.

https://doi.org/10.1017/S1759078725000546 Published online by Cambridge University Press

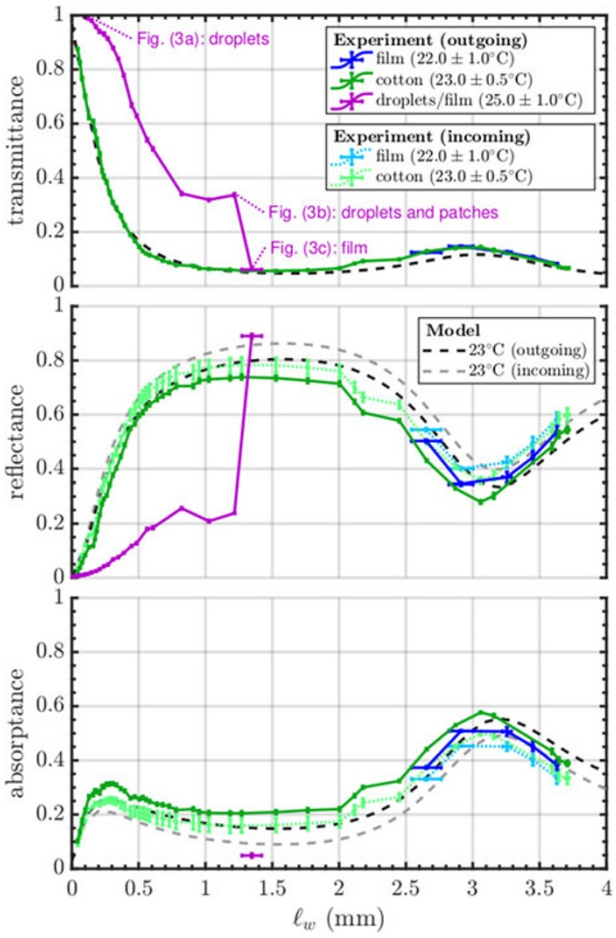


Figure 6. Measured transmittance, reflectance, and absorptance of the wet radome, see Eq. (2), averaged between 5450 ± 50 MHz, as a function of the computed water layer thickness, ℓ_w. The outgoing quantities $|\mathcal{T}|^2$, $|\mathcal{R}|^2$, and $|\mathcal{A}|^2$ (represented by solid dark lines) and incoming quantities $|\mathcal{T}'|^2$, $|\mathcal{R}'|^2$, and $|\mathcal{A}'|^2$ (dotted light lines) are measured. Data are collected from three different experiments. In the "film" experiment (blue), thick water films are tested. In the "cotton" experiment (green), a thin cotton tissue is used to mimic thin water films on the hydrophobic radome surface. In the "droplets/film" experiment without the tissue (purple), the water forms droplets (Figure 3a and 3b). When there is lots of water on the radome, the droplets can be smeared out to a film (Figure 3c). The measurements are compared with the outgoing (dashed black) and incoming (dashed gray) quantities predicted by the analytical plane wave model from Section "Analytical model for flat radome", calculated for frequency $\nu = 5450$ MHz and water temperature $T = 23$°C.

The discrepancies between the measured and modeled transmittance (and consequently the absorptance) might partly be explained by diffraction at the edges of the radome, and by the superposition of standing wave effects between the antennas, and between antennas and radome.

Applying Eq. (3) for the 3.25 m radius radome of the Swiss weather radars, at $T = 23 \pm 0.5$°C the computed water thicknesses given in Fig. 5 corresponds to the rain rates $R = 0.038 \pm 0.001$ mm/h (drizzle), 0.641 ± 0.008 mm/h (light rain), 3.51 ± 0.05 mm/h (moderate rain), and 89 ± 1 mm/h (heavy rain).

Scattering parameters at the working frequencies of the Swiss weather radars

In this section, we focus on the frequencies relevant for the Swiss weather radars. Figure 6 shows the measured transmittance, reflectance, and absorptance of the wet radome, averaged over the 5400–5500 MHz range (17 frequency channels with 6.25 MHz spacing) in the outgoing direction ($|\mathcal{T}|^2$, $|\mathcal{R}|^2$, $|\mathcal{A}|^2$ – continuous dark lines) and in the incoming direction ($|\mathcal{T}'|^2$, $|\mathcal{R}'|^2$, $|\mathcal{A}'|^2$ – dotted light lines), as a function of the computed water layer thickness, ℓ_w.

The figure shows measurements from three experiments described in Section "Description of the measurements — Simulating a rain coverage in the laboratory": "film" (blue), "cotton" (green), and "droplets/film" (purple). Similar data of the experiment "droplets/film" were previously shown in [51]. The lines connect the mean values of the 17 measurements at each water amount. Vertical bars represent their standard deviation. The horizontal error bars indicate the uncertainty in the computed water film thickness but do not account for the presence of a tissue. The three experiments are performed within a temperature range of about three degrees over which the analytical model remains almost unchanged. We present the computation at a frequency $\nu = 5450$ MHz and a water temperature $T = 23$°C, for the outgoing (dashed black) and incoming directions (dashed gray). The complex permittivity of pure water at the specified frequency and temperature is $\epsilon_d = 73.06 - 20.23i$ [63].

In the "film" experiment (blue), the measured transmittance, reflectance, and thus absorptance are in satisfactory agreement with the model, for both the outgoing (continuous dark blue) and incoming directions (dotted light blue). In particular, note the consistent difference in reflectance from the two sides of the radome, between model and experiment. As mentioned in Section "Analytical model for flat radome", this difference is characteristic for nonsymmetric and for lossy multilayers such as wet radomes.

In the "cotton" experiment (green), we used a cotton tissue on the radome to mimic thin water films (green). The measured transmittance agrees well with the simulation, and the reflectance also shares the key characteristics of the model. The few abrupt irregularities in the measurements might result from a nonuniform distribution of the water.

Both in the "film" and in the "cotton" experiments, the measurements are horizontally and vertically displaced compared to the analytical model. Referencing to Sections "Description of the measurements — Accuracy of the calibration method" and "Description of the measurements — Poynting's theorem in the experiments", the vertical offsets may result from refractive bias relative to calibration. This effect would be most pronounced if the radome were bent, forming a plano-convex water lens. The bending also causes an excess of water in the center of the radome and accordingly shifts the Fabry–Pérot interference pattern compared to a uniform water film. Considering the maximum (minimum) in transmittance (reflectance) for water layers of thickness $\ell_w \sim 3$ mm, the offset is between 0.1 mm and 0.2 mm. The same result is obtained by fitting the power spectra of the scattering parameters. In the "cotton" experiment, an additional bias of 0.052 ± 0.0006 mm due to the tissue (product of its thickness and solid volume fraction in Table 2) needs to be considered.

In the "droplets/film" experiment (purple), only scattering in the outgoing direction was measured (see Fig. 3 and Section "Description of the measurements — Calibration"). Due to the spacing between the droplets, the transmittance is higher, and the reflectance is lower than in the analytical model for a water film (black dashed line). A thorough analysis would include characterizing the radome surface [5, 11], as well as the size and spatial distribution of the droplets [13, 38, 40]. Provided that the droplets are sufficiently small and close to each other with respect to the

https://doi.org/10.1017/S1759078725000546 Published online by Cambridge University Press

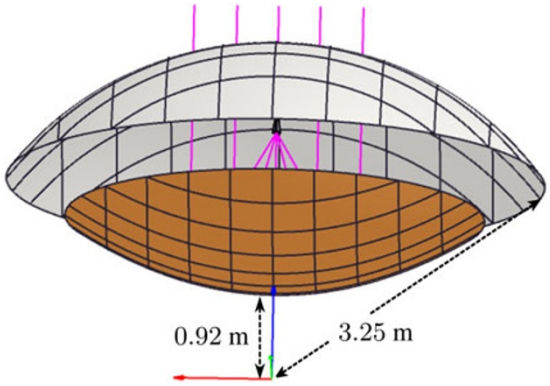


Figure 7. Schematic of the Swiss weather radar geometry, including a spherical radome with 3.25 m outer radius (gray), a 4.05 m parabolic reflector with 1.524 m focal length (brown), and a focal-point feed (black) with geometrical optics rays emanating from it (magenta). The reflector surface has a 0.92 m offset to the center of the radome, corresponding to the origin of the indicated Cartesian coordinate system (red-green-blue).

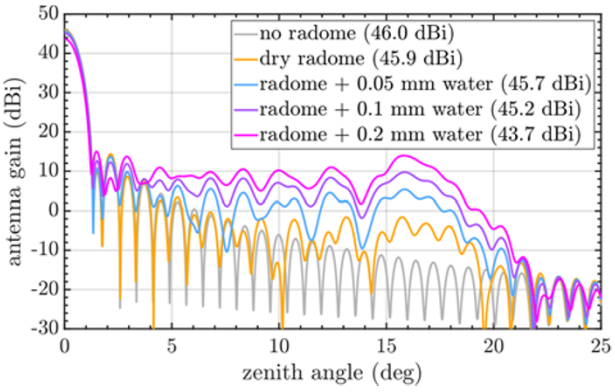


Figure 8. GRASP Physical Optics simulation of the Swiss weather radars' antenna gain at the frequency $\nu = 5450$ MHz, expressed in decibels relative to an isotropic radiator as a function of the zenith angle. Shown are simulations with no radome (gray), dry radome (yellow), and wet radome with water films of thickness 0.05 mm (blue), 0.1 mm (purple), and 0.2 mm (magenta). The legend provides the antenna peak gain for each simulations.

wavelength, the scattering properties of the water layer can be approximated with an *effective* dielectric model [57, pp. 464–496]. In general, however, the situation with droplets is a more miscellaneous scattering problem than the specular one for water films, including directions other than the antenna boresight [68, pp. 61, 381]. In that case, in Fig. 6, the terms transmittance and reflectance represent the fractions of power that are scattered along and against the direction of the incident wave (forward- and backscatter). Additional measurements from different angles would be needed to estimate the fraction of power that is absorbed in the wet radome. Smearing out the water to a film (Fig. 3c) reduced the transmittance and increased the reflectance by 6 dB. The results align with the model, and the absorbed fraction of power is computed with Eq. (2) like for the other experiments. The small offset in reflectance could come from the calibration.

Physical Optics antenna simulations

In the previous sections, we considered a simplified setup with a planar radome illuminated by a uniform plane wave (see the experiment setup shown in Fig. 2 and the analytical model explained in Section "Analytical model for flat radome"). Using Physical Optics simulations with the software package GRASP, here we investigate the influence of the radome's curvature, including multiple reflections of the signal between antenna and radome. The setup in Fig. 7 is representative of the Swiss weather radars in Fig. 1, including parabolic reflector (brown), focal-point feed (black), and spherical radome with the composition described in Table 1 (gray). The reflector is modeled as an ideal parabolic mirror, and the feed is assumed to radiate a linearly polarized Gaussian beam with a −12 dB edge taper on the reflector. The radome is treated as a single piece, not taking into account the presence and geometric distribution of panels and joints [69]. Blockage and scattering by feed and struts are also excluded from the simulation.

Figure 8 shows the simulated antenna pattern at 5450 MHz in the feed's polarization plane, with no (gray), dry (yellow), and wet radome (blue, purple, magenta) with water films of uniform thicknesses $\ell_w = 0.052$ mm, $\ell_w = 0.1$ mm, and $\ell_w = 0.2$ mm, respectively, as suggested by Eq. (3). We consider pure water at temperature $T = 23$°C, as in the experiments. The simulations account for one additional reflection of the signal between radome and reflector. Higher-order reflections are not considered.[1] Similar simulations at the temperature $T = 25$°C are provided in [51]. The results show a reduction in antenna peak gain due to absorption and reflection at the wet radome. The reflected wave is refocused by the spherical radome toward the parabolic reflector, which again redirects it outward. Depending on the relative positions of the focal points of the parabolic reflector and of the spherical radome, the reflections contribute appreciably to the sidelobes. In our case, the reflector is approximately 0.8 m too close to the radome for the foci to coincide.

Referring to Eq. (3), for the 3.25 m radius radome of the Swiss weather radars, at $T = 23$°C the water film thicknesses correspond to the rain rates $R \approx 1.0$ mm/h (light rain), $R \approx 7.9$ mm/h (moderate rain), and $R \approx 61.5$ mm/h (heavy rain). If we instead consider $T = 1$°C, due to the increased kinematic viscosity at lower temperatures, water films of the same thickness are expected for $R \approx 0.5$ mm/h, $R \approx 4.2$ mm/h, and $R \approx 33.4$ mm/h. The complex permittivity of pure water at $\nu = 5450$ MHz and $T = 1$°C is $\epsilon_d = 66.41 - 35.81i$ [63]. The simulated antenna patterns at this temperature are similar to those at $T = 23$°C and vary only marginally over the frequency range relevant for the Swiss weather radars (not shown). The increase in sidelobe agrees with empirical evidence at C-band from [5]. Finally, the multiple reflections toward the cold sky imply a smaller increase of the antenna temperature compared to a geometry where the reflections are terminated in an ambient-temperature environment inside of the radome. See [7] for reference.

Conclusions and outlook

We investigate the scattering parameters of the spherical radome of the Swiss weather radars (Fig. 1), both with and without water on the radome. Measurements are performed from 3.5 GHz through 7 GHz, using a simplified setup with a planar replica of the real radome, vertically centered in a horizontal position, between two standard gain horns connected to a two-port vector network analyzer (Fig. 2). Deionized water is used. The data are calibrated with dedicated measurements taken without the radome. The results are compared with an analytical model for uniform plane wave incidence on radome and a water film of uniform thickness (Section "Analytical model for flat radome").

https://doi.org/10.1017/S1759078725000546 Published online by Cambridge University Press

Satisfactory agreement is found for the reflectance of the dry radome replica. We also verify that the dielectric properties of its foam core comply with manufacturer specifications for the actual radome (Fig. 4).

The radome replica has a hydrophobic coating, causing the water to accumulate in droplets (Fig. 3), resulting in higher forward- and lower backscatter compared to water films [51]. However, water films thicker than approximately 1 mm can be created, and in that case, we find good agreement with the model (Fig. 6). Because the radome refractively focuses the electromagnetic field in the experiment, the measurements are biased with respect to calibration (see Sections "Description of the measurements — Accuracy of the calibration method" and "Description of the measurements — Poynting's theorem in the experiments"). Moreover, we observe that the radome bends slightly under the weight of the thicker water layers, increasing the height of the water column in the center of the radome by about 0.1–0.2 mm for water layer thickness $\ell_w \sim 3$ mm. This results in a shift of the Fabry–Pérot interference pattern compared to the same amount of water distributed as a uniform film. For the meteorologically realistic thin water films, both refraction and bending are of minor importance.

To empirically simulate thin water films, we place fine hygroscopic cotton and silk tissues on the radome. The results agree well with the simple model (Figs. 5 and 6). Given that radomes tend to lose their hydrophobic virtue with aging and might even develop moss on the shady side, the experiments with the tissues could represent such situations.

Physical Optics simulations with GRASP for a representative setup of the Swiss weather radars (Fig. 7) show that multiple reflections between the spherical radome and the parabolic reflector result in a wide sidelobe and that a significant fraction of the reflected wave still terminates on the cold sky (Fig. 8). The simulations could be further refined by accounting for the influence of the four struts that hold the feed, the blockage of the feed, a more realistic feed pattern, and the scattering due to the joints between the radome panels. It would be useful to experimentally verify the antenna pattern of the weather radars.

The horizontally positioned flat radome replica is designed to empirically study static rivulet configurations with a controlled amount and distribution of water on the radome. Preliminary polarimetric scattering measurements indicate that diffraction effects can be observed for a grating of rivulets on the radome.

Acknowledgements. We thank in particular Urs Germann from MeteoSwiss and Christian Theiler from EPFL for their support. The measurements were performed in the anechoic chamber of armasuisse Science and Technology. Many thanks to Christoph von Rohr from armasuisse for his support during the test campaign. Philipp J. Schmid also thanks Marc Schneebeli and Andreas Leuenberger for their valuable inputs, Lorenzo Ciorba for the useful discussions, and Simona Procacci for carefully reading the manuscript. Moreover, special thanks belong Anton Güdel for his assistance in building the wooden scaffold for the experiments.

Competing interests. The authors declare none.

Note

1. Using a 64-bit architecture with twelve i5-12500 CPU cores and 16 GB RAM, in TICRA Tools 23.1, the simulation without the radome takes of the order of 10 s. The simulations with radome last about 4 min.

References

1. **Germann U, Boscacci M, Clementi L, Gabella M, Hering A, Sartori M, Sideris I and Calpini B** (2022) Weather Radar in Complex Orography. *Remote Sensing* **14**(3), 1–40, article no. 503. doi: 10.3390/rs14030503.
2. **Skolnik MI** (2008) *Radar Handbook*. 3rd Edn. McGraw-Hill's AccessEngineering. New York (NY, USA): McGraw-Hill Education.
3. **Kozakoff DJ** (2010) *Analysis of radome-enclosed antennas*. 2nd Edn. Artech House antennas and propagation library. Norwood (MA, USA): Artech House.
4. **Blevis B** (1965) Losses due to rain on radomes and antenna reflecting surfaces. *IEEE Transactions on Antennas and Propagation* **13**(1), 175–176. doi: 10.1109/TAP.1965.1138384.
5. **Punnett MB** (1972) Utilization of hydrophobic materials for air inflated radomes. *Journal of Coated Fibrous Materials* **1**(3), 162–179. doi: 10.1177/152808377200100303.
6. **Dijk J, Maanders EJ and v. d. Vorst A** (1973) The measurement of noise temperatures of dry and wet radomes. In *3rd European Microwave Conference (04–07 September 1973)*. Vol. 2. Brussels (BE): IEEE, 1–4. doi: 10.1109/EUMA.1973.331690.
7. **Chang KC** (1986) System performance in rain in a radome-enclosed environment. *International Journal of Infrared and Millimeter Waves* **7**(2), 267–289. doi: 10.1007/BF01013271.
8. **Germann U** (1999) Radome attenuation – a serious limiting factor for quantitative radar measurements? *Meteorologische Zeitschrift* **8**(3), 85–90. doi: 10.1127/metz/8/1999/85.
9. **Anderson I** (1975) Measurements of 20-GHz transmission through a radome in rain. *IEEE Transactions on Antennas and Propagation* **23**(5), 619–622. doi: 10.1109/TAP.1975.1141134.
10. **Siller C** (1979) Preliminary testing of teflon as a hydrophobic coating for microwave radomes. *IEEE Transactions on Antennas and Propagation* **27**(4), 555–557. doi: 10.1109/TAP.1979.1142132.
11. **Effenberger JA, Strickland RR and Joy EB** (1986) The effects of rain on a radome's performance. *Microwave Journal* **29**(5), 261–272.
12. **Dietrich FJ and West DB** (1988) An experimental radome panel evaluation. *IEEE Transactions on Antennas and Propagation* **36**(11), 1566–1570. doi: 10.1109/8.9706.
13. **Salazar-Cerreño JL, Chandrasekar V, Trabal JM, Siquera P, Medina R, Knapp E and McLaughlin DJ** (2014) A Drop Size Distribution (DSD)-Based Model for Evaluating the Performance of Wet Radomes for Dual-Polarized Radars. *Journal of Atmospheric and Oceanic Technology* **31**(11), 2409–2430. doi: 10.1175/JTECH-D-13-00208.1.
14. **Cohen A, Hogg D and Chu T** (1976) Comments on "The role of rain in satellite communications". *IEEE Transactions on Antennas and Propagation* **24**(6), 903–904. doi: 10.1109/TAP.1976.1141458.
15. **Shao W, Kan Q, Bai X and Wang C** (2022) Robust Superhydrophobic Coatings for Enhanced Corrosion Resistance and Dielectric Properties. *Coatings* **12**(11), 1–11, article no. 1655. doi: 10.3390/coatings12111655.
16. **Wei J, Zhang J, Cao X, Huo J, Huang X and Zhang J** (2023) Durable superhydrophobic coatings for prevention of rain attenuation of 5G/weather radomes. *Nature Communications* **14**(1), 1–9, article no. 2862. doi: 10.1038/s41467-023-38678-0.
17. **Ulaby FT and Long DG** (2014) *Microwave Radar and Radiometric Remote Sensing*. Ann Arbor (MI, USA): University of Michigan Press.
18. **Joss J** (1996) Radome: Attenuation and Phase-shift. In *10th meeting of COST (European Union Coperation in Science and Technology) 75: "Advanced Radar Systems"*. Document for Working Group 1 (Advanced data processing with conventional and future radars). Brussels (BE).
19. **Gibble D** (1964) Effect of rain on transmission performance of a satellite communication system. In *IEEE International Convention Record*. Vol. Part VI (Radio communication; Recording and Audio; Television), 52. doi: 10.1109/MSPEC.1965.5531868.
20. **Guo X and Mei CC** (2019) Liquid film on a hydrophobic radome or roof top in rain. *Journal of Fluid Mechanics* **870**(7), 1158–1174. doi: 10.1017/jfm.2019.319.
21. **Ruze J** (1965) More on wet randomes. *IEEE Transactions on Antennas and Propagation* **13**(5), 823–824. doi: 10.1109/TAP.1965.1138492.

https://doi.org/10.1017/S1759078725000546 Published online by Cambridge University Press

22. **Hogg DC and Chu TS** (1975) The role of rain in satellite communications. *Proceedings of the IEEE* **63**(9), 1308–1331. doi: 10.1109/PROC.1975.9940.
23. **Merceret FJ and Ward JG** (2002) *Attenuation of weather radar signals due to wetting of the radome by rainwater or incomplete filling of the beam volume*. Technical Memorandum. NASA/Kennedy Space Center, 1–9, report no. NASA/TM—2002–211171. Available at: https://ntrs.nasa.gov/citations/20020043890 (accessed 23 May 2025).
24. **Bechini R, Cremonini R, Gorgucci E and Baldini L** (2006) Dual-pol radar calibration and correction of the bias introduced by non uniform radome wetting. In *4th European Conference on Radar in Meteorology (ERAD, 18–22 September 2006)*. Barcelona (ES), 593–596. Available at: https://www.researchgate.net/publication/265383558_Dual-pol_radar_calibration_and_correction_of_the_bias_introduced_by_non_uniform_radome_wetting (accessed 23 May 2025).
25. **Schneebeli M, Sakuragi J, Biscaro T, Angelis CF, Carvalho da Costa I, Morales C, Baldini L and Machado LAT** (2012) Polarimetric X-band weather radar measurements in the tropics: radome and rain attenuation correction. *Atmospheric Measurement Techniques* **5**(9), 2183–2199. doi: 10.5194/amt-5-2183-2012.
26. **Frasier SJ, Kabeche F, Figueras i Ventura J, Al-Sakka H, Tabary P, Beck J and Bousquet O** (2013) In-Place Estimation of Wet Radome Attenuation at X Band. *Journal of Atmospheric and Oceanic Technology* **30**(5), 917–928. doi: 10.1175/JTECH-D-12-00148.1.
27. **Cohen A and Smolski A** (1966) The effect of rain on satellite communications earth terminal rigid radomes. *Microwave Journal* **9**(9), 111–121.
28. **Ruze J** (1967) Effect of rain on radome performance. In *A large radio-radar telescope – CAMROC design concepts*. Committee Members of Harvard University, M.I.T., M.I.T. Lincoln Laboratory, and Smithsonian Astrophysical Observatory (ed). Vol. 2. Cambridge (MA, USA): Cambridge Radio Observatory Committee. Chap. Annex 2.
29. **Moeller AW and Willey RE** (1982) *Investigation of Hydrophobic Radomes for Microwave Landing System: Final Report*. Final Report. Washington, D.C. (USA): Unites States Federal Aviation Administration, Program Engineering & Maintenance Service, 1–39, report no. DOT/FAA/RD–82/87. Available at: https://apps.dtic.mil/sti/citations/ADA125689 (accessed 23 May 2025).
30. **Hendrix CE, McNally JE and Monzingo RA** (1989) Depolarization and attenuation effects of radomes at 20 GHz. *IEEE Transactions on Antennas and Propagation* **37**(3), 320–328. doi: 10.1109/8.18728.
31. **Fenn AJ** (1997) Measurements of wet radome transmission loss and depolarization effects in simulated rain at 20 GHz. In *10th International Conference on Antennas and Propagation (ICAP, 14–17 April 1997)*. Vol. 1. Edinburgh (UK): The Institution of Engineering & Technology, 474–477. doi: 10.1049/cp:19970298.
32. **Löffler-Mang M and Gysi H** (1998) Radome attenuation of C-band Doppler radar as a function of rain characteristics. In *COST 75 : Advanced Weather Radar Systems : International Seminar (Palazzo Società Elettrica Sopracenerina, Locarno, Switzerland, 23–27 March 1998)*. Collier C (ed). Luxembourg: Office for Official Publications of the European Communities, 520–526. Available at: https://op.europa.eu/en/publication-detail/-/publication/404fb559-9d41-4002-a7e0-9a08c81fd264 (accessed 23 May 2025).
33. **Arage A, Kuehnle G and Jakoby R** (2006) Measurement of wet antenna effects on millimetre wave propagation. In *2006 IEEE Conference on Radar (24–27 April 2006)*. Verona (NY, USA), 190–194. doi: 10.1109/RADAR.2006.1631796.
34. **Kurri M and Huuskonen A** (2008) Measurements of the Transmission Loss of a Radome at Different Rain Intensities. *Journal of Atmospheric and Oceanic Technology* **25**(9), 1590–1599. doi: 10.1175/2008JTECHA1056.1.
35. **Bechini R, Chandrasekar V, Cremonini R and Lim S** (2010) Radome attenuation at X-band radar operations. In *6th European Conference on Radar in Meteorology and Hydrology (ERAD, 6–10 September 2010)*. Sibiu (RO).
36. **Chen N, Gourova R, Krasnov O and Yarovoy A** (2017) The influence of the water-covered dielectric radome on 77 GHz automotive radar signals. In *European Radar Conference (EURAD, 11–13 October 2017)*. Nuremberg DE, 139–142. doi: 10.23919/EURAD.2017.8249166.
37. **Mancini A, Salazar JL, Lebrón RM and Cheong BL** (2018a) A Novel Instrument for Real-Time Measurement of Attenuation of Weather Radar Radome Including Its Outer Surface. Part II: Applications. *Journal of Atmospheric and Oceanic Technology* **35**(5), 975–991. doi: 10.1175/JTECH-D-17-0084.1.
38. **Norouzian F, Du R, Hoare EG, Gardner P, Constantinou C, Cherniakov M and Gashinova M** (2018) Low-THz Transmission Through Water-Containing Contaminants on Antenna Radome. *IEEE Transactions on Terahertz Science and Technology* **8**(1), 63–75. doi: 10.1109/TTHZ.2017.2778498.
39. **Mancini A, Lebrón RM and Salazar JL** (2019) The Impact of a Wet S-Band Radome on Dual-Polarized Phased-Array Radar System Performance. *IEEE Transactions on Antennas and Propagation* **67**(1), 207–220. doi: 10.1109/TAP.2018.2876733.
40. **Bouquin P, Bourreau D and Peden A** (2024) Millimeter and Submillimeter Wave Transmission Through a Radome Covered by Water: The Impact of the Shape of Water. *Journal of Infrared, Millimeter, and Terahertz Waves* **45** (3), 265–279. doi: 10.1007/s10762-024-00969-y.
41. **Moroder C, Siart U, Chwala C and Kunstmann H** (2020) Modeling of Wet Antenna Attenuation for Precipitation Estimation From Microwave Links. *IEEE Geoscience and Remote Sensing Letters* **17**(3), 386–390. doi: 10.1109/LGRS.2019.2922768.
42. **Mancini A, Salazar JL, Lebrón RM and Cheong BL** (2018b) A Novel Instrument for Real-Time Measurement of Attenuation of Weather Radar Radome Including Its Outer Surface. Part I: The Concept. *Journal of Atmospheric and Oceanic Technology* **35**(5), 953–973. doi: 10.1175/JTECH-D-17-0083.1.
43. **Giger AJ** (1965) 4-gc transmission degradation due to rain at the andover, maine, satellite station. *The Bell System Technical Journal* **44**(7), 1528–1533. doi: 10.1002/j.1538-7305.1965.tb04192.x.
44. **Abraham Z and Kokubun F** (1992) Calibration of radioastronomical observations in the presence of a radome. *Astronomy and Astrophysics* **257**(2), 831–834. Available at: https://ui.adsabs.harvard.edu/abs/1992A%26A...257..831A/abstract (accessed 23 May 2025).
45. **Thompson R, Illingworth A and Ovens J** (2011) Emission: a simple new technique to correct rainfall estimates from attenuation due to both the radome and heavy rainfall. In *International Symposium on Weather Radar and Hydrology (WRaH, 18–21 April 2011)*. Exeter (UK), 39–44. Available at: https://centaur.reading.ac.uk/31018/ (accessed 23 May 2025).
46. **Thompson R and Illingworth A** (2012) *Correcting attenuation in operational radars from both heavy rain and the radome using the observed microwave emission*. 7th European Conference on Radar in Meteorology and Hydrology (ERAD, 24–29 June 2011). Toulouse (FR). Available at: http://www.meteo.fr/cic/meetings/2012/ERAD/presentations/wednesday/8A-5.pdf (accessed 23 May 2025).
47. **Thompson R, Illingworth A and Darlington T** (2013) *Correcting for attenuation: Can Emission Provide an Absolute Constraint?* 36th AMS Radar Conference (16–20 September 2013). Breckenridge (CO, USA). Available at: https://ams.confex.com/ams/36Radar/webprogram/Paper228722.html (accessed 23 May 2025).
48. **Schneebeli M and Berne A** (2012) An Extended Kalman Filter Framework for Polarimetric X-Band Weather Radar Data Processing. *Journal of Atmospheric and Oceanic Technology* **29**(5), 711–730. doi: 10.1175/JTECH-D-10-05053.1.
49. **Gorgucci E, Bechini R, L. B, Cremonini R and Chandrasekar V** (2013) The Influence of Antenna Radome on Weather Radar Calibration and Its Real-Time Assessment. *Journal of Atmospheric and Oceanic Technology* **30**(4), 676–689. doi: 10.1175/JTECH-D-12-00071.1.
50. **Mancini A, Salazar JL, Lebrón RM and Cheong BL** (2017) A novel technique to characterize the effect of rain over a radome for radar applications. In *IEEE Radar Conference (RadarConf, 08–12 May 2017)*. Seattle (WA, USA): IEEE, 0470–0475. doi: 10.1109/RADAR.2017.7944249.
51. **Schmid PhJ, Sartori M, Gabella M, Renker M, Kotiranta M and Murk A** (2024) Measuring and Modelling the Scattering Parameters of the Wet Radome of the Swiss Weather Radars. In *2024 18th European Conference*

https://doi.org/10.1017/S1759078725000546 Published online by Cambridge University Press

on Antennas and Propagation (EuCAP, 17–22 March 2024). Glasgow (UK): IEEE, 1–5. doi: 10.23919/EuCAP60739.2024.10501002.
52. **Collin RE** (2001) *Foundations for microwave engineering*. Dudley DG (ed). 2nd Edn. IEEE Press series on electromagnetic wave theory. Hoboken (NJ, USA): John Wiley & Sons.
53. **Collin RE** (1991) *Field theory of guided waves*. Dudley DG (ed). 2nd Edn. IEEE Press series on electromagnetic wave theory. New York (NY, USA): Wiley-IEEE Press.
54. **Gerhart PM, Gerhart AL and Hochstein JI** (2018) *Munson, Young and Okiishi's Fundamentals of Fluid Mechanics*. 8th Edn. Hoboken (NJ, USA): John Wiley & Sons.
55. **Oron A, Davis SH and Bankoff SG** (1997) Long-scale evolution of thin liquid films. *Reviews of modern physics* **69**(3), 931–980. doi: 10.1103/RevModPhys.69.931.
56. **Torgovnikov GI** (1993) *Dielectric Properties of Wood and Wood-Based Materials*. Timell TE (ed). 1st Edn. Springer Series in Wood Science. Berlin: Springer. doi: 10.1007/978-3-642-77453-9.
57. **Mätzler C** (2006) *Thermal microwave radiation: applications for remote sensing*. Clarricoats PJB and Jull EV (eds). Vol. 52. IET electromagnetic waves series. Herts (UK): The Institution of Engineering & Technology.
58. **Mrnka M, Appleby R and Saenz E** (2022) Accurate S-Parameter Modeling and Material Characterization in Quasi-Optical Systems. *IEEE Transactions on Terahertz Science and Technology* **12**(2), 199–210. doi: 10.1109/TTHZ.2021.3140201.
59. **Rolfes I and Schiek B** (2004) Calibration methods for microwave free space measurements. *Advances in Radio Science* **2**(5), 19–25. doi: 10.5194/ars-2-19-2004.
60. **Goldsmith PF** (1998) *Quasioptical systems: Gaussian beam quasioptical propagation and applications*. Anderson JB (ed). 1st Edn. Vol. 4. IEEE Press/Chapman & Hall Publishers Series on Microwave Technology and RF. Piscataway (NJ, USA): Wiley-IEEE Press.
61. **Sharkov EA** (2003) *Passive microwave remote sensing of the earth: physical foundations*. 1st Edn. Springer-Praxis Books in Geophysical Sciences. Berlin: Springer.
62. **Von Hippel AR** (1995) *Dielectrics and waves*. 2nd Edn. The Artech House microwave library. Boston (MA, USA): Artech House.
63. **Meissner T and Wentz F** (2004) The complex dielectric constant of pure and sea water from microwave satellite observations. *IEEE Transactions on Geoscience and Remote Sensing* **42**(9), 1836–1849. doi: 10.1109/TGRS.2004.831888.
64. **Mukai Y and Suh M** (2020) Relationships between structure and microwave dielectric properties in cotton fabrics. *Materials Research Express* **7**(1), 1–12, article no. 015105. doi: 10.1088/2053-1591/ab653c.
65. **Yamada Y** (2022) Dielectric Properties of Textile Materials: Analytical Approximations and Experimental Measurements—A Review. *Textiles* **2**(1), 50–80. doi: 10.3390/textiles2010004.
66. **Dhupkariya S, Singh VK and Shukla A** (2014) A Review of Textile Materials for Wearable Antenna. *Journal of Microwave Engineering & Technologies* **1**(3), 7–14.
67. **Sihvola A** (1999) *Electromagnetic Mixing Formulas and Applications*. Vol. 47. IEEE electromagnetic waves series. Herts (UK): The Institution of Engineering & Technology. doi: 10.1049/PBEW047E.
68. **Bohren CF and Huffman DR** (1983) *Absorption and scattering of light by small particles*. New York (NY, USA): John Wiley & Sons.
69. **Manz A and Monk T** (1998) Radome Effects on Weather Radar Systems. In *COST 75 : Advanced Weather Radar Systems : International Seminar (Palazzo Società Elettrica Sopracenerina, Locarno, Switzerland, 23–27 March 1998)*. Collier C (ed). Luxembourg: Office for Official Publications of the European Communities, 467–478. Available at: https://op.europa.eu/en/publicationdetail/-/publication/404fb559-9d41-4002-a7e0-9a08c81fd264 (accessed 23 May 2025).



Philipp J. Schmid received his MSc degree in physics from EPFL, Switzerland, in 2022. He started investigating wet radome effects during an internship at the Federal Office of Meteorology and Climatology MeteoSwiss. Before starting his PhD at the Institute of Applied Physics of the University of Bern in autumn 2023, he developed automated calibration procedures for weather radar target simulators at Palindrome Remote Sensing GmbH, Landquart, Switzerland.



Maurizio Sartori received his diploma in Natural Science from ETH in Zurich, Switzerland, in 1993, and the PhD degree at the Institute of Geophysics, ETH Hönggerberg, in 2000 (The Quaternary climate in loess sediments: Evidence from rock and mineral magnetic and geochemical analysis). From 2000 to 2009, he worked for armasuisse Science and Technology in Bern, Switzerland, mainly on acceptance testing of remote sensing systems in the microwave frequency range. In 2010, he joined the Radar, Satellite and Nowcasting division at MeteoSwiss in Locarno-Monti, Switzerland, the group responsible for the renewal of the Swiss weather radar network and for the operation of the five new polarimetric Doppler weather radars. Maurizio is co-responsible for all matters relating to the operation, maintenance, calibration, monitoring, and continuous renewal of the radar hardware.



Marco Gabella received a PhD in Remote Sensing in 1995 from Politecnico di Torino, Italy, where he became assistant professor in 2001. In 2008, he joined the Radar, Satellite and Nowcasting division at MeteoSwiss in Locarno-Monti, Switzerland. His fields of activities in research and technological development include electromagnetic wave propagation and remote sensing of the atmosphere at optical and microwave frequencies. His main focus concerns space-borne and ground-based weather radar. The scientific activity is documented by more than 70 publications on peer-reviewed international journals and a few book chapters.



Matthias Renker holds a degree in mechanical engineering and an MSc degree in physics, as well as a PhD in physics in the field of THz optics. Since 2014, he has been working in the field of radars and mini drones and counter drone technology for armasuisse Science and Technology, Switzerland.



Daniel Wolfensberger holds a MSc degree in Environmental Engineering from EPFL, where he completed both a master's thesis in radar meteorology and a subsequent PhD. His doctoral research focused on the detection and characterization of the melting layer in precipitation and the development of a polarimetric forward radar operator. Following his PhD, Daniel undertook a joint postdoctoral position between EPFL and MeteoSwiss, where he developed a novel quantitative precipitation estimation (QPE) algorithm using a random forest approach. Currently, he is part of the Radar, Satellite and Nowcasting division at MeteoSwiss in Locarno-Monti, with responsibilities including the management of a mobile X-band radar system.

https://doi.org/10.1017/S1759078725000546 Published online by Cambridge University Press



Mikko Kotiranta received the MSc (Tech.) degree (Hons.) in electrical engineering from the Helsinki University of Technology, Espoo, Finland, in 2008, and the PhD degree in physics from the Goethe University of Frankfurt, Frankfurt am Main, Germany, in 2013. He was with the Fraunhofer Institute for Applied Solid State Physics IAF, Freiburg im Breisgau, Germany, from 2013 to 2015, as a Monolithic Microwave Integrated Circuit (MMIC) Designer and, from 2014, as the Head of the Device Modeling Group. He was involved in the design and modeling of microwave and millimeter-wave MMICs for astronomical and space applications. In 2015, he joined the Institute of Applied Physics, University of Bern, Bern, Switzerland, where he is currently engaged in the development quasi-optics and calibration targets for ground- and space-based instruments operating from microwave to terahertz frequencies.



Axel Murk received the MSc degree in physics from the Technical University of Munich, Munich, Germany, in 1995, and the PhD degree in physics from the University of Bern, Bern, Switzerland, in 1999. Since 1999, he has been involved in the development and characterization of submillimeter-wave instrumentation for different ground-based and space-borne projects. In 2003, he joined the Japan Aerospace Exploration Agency, as an Invited Scientist. Since 2006, he has been the Head of the Terahertz Optics Group, Institute of Applied Physics, University of Bern. His current research interests include antenna design and measurements at frequencies in the millimeter and submillimeter-wave range, quasi-optics, remote sensing, and radio astronomical instrumentation.

https://doi.org/10.1017/S1759078725000546 Published online by Cambridge University Press